By-products revaluation in the production of design micaceous materials

Anais Mouchet [a], Florian Raffin [b], Agustín Cota [c], Francisco J. Osuna [d], Esperanza Pavón [d,e], María D. Alba [d,*]

[a] Université de Pau et des Pays de l'Adpor (UPPA), Avenue de l'Université - BP 576, 64012 Pau, France
[b] Chimie ParisTech, PSL University, Institut de Recherche de Chimie Paris, 11 rue Pierre et Marie Curie, 75005 Paris, France
[c] Centro de Investigación, Tecnología e Innovación de la Universidad de Sevilla, Avda. Reina Mercedes, 4b, 41012 Sevilla, Spain
[d] Instituto Ciencia de los Materiales de Sevilla (CSIC-US), Avda. Americo Vespucio, 49, 41092 Sevilla, Spain
[e] Departamento de Física de la Materia Condensada, Universidad de Sevilla, Avda. Reina Mercedes, s/n, 41012 Sevilla, Spain

ARTICLE INFO

ABSTRACT

One of the main objectives of a sustainable development and circular economy is the recycling of by-products generated in industrial and agricultural production processes. One of the possible solution is the use of such by-product materials in the synthesis of environmental adsorbents. In the current research, we present the synthesis of a high charge swelling mica with enhance adsorbent properties from blast furnace slag and rice husk ash. Moreover, to ensure the sustainable synthesis a natural bentoniteis used as Si and Al source. Thus, the current study investigated the fabrication of swelling high charged micas, Na-Mn (n (layer charge) = 2 or 4), from FEBEX bentonite, blast furnace slag and rice husk ash thorough the NaCl melt method. The reaction yield, cation framework distribution and structural characteristic of micas have been studied thorough X-ray Diffraction and Solid State Nuclear Magnetic Resonance. The yields of Na-Mn synthesis and degree of purity of the mica depends on the nature of these precursors. Thus, a sustainable, non-expensive and environmental friendly process has been evaluated.

1. Introduction

The growing concern about environmental pollution has resulted in an increase in the research and the development of sustainable technologies. Thus, sustainable development is an important matter worldwide and it takes into consideration all environmental, economic and social aspects (Elkington, 1999; Chen et al., 2020). In particular, one of the main objectives is to get the best use of natural resources with the minimum cost of energy and the minimum (and if possible null) formation of by-products.

However, vast amounts of by-products are produced as consequence of industrial and agricultural production processes (Xie et al., 2016; Zhang et al., 2018). Limitations related to the storage of these solid wastes and other environmental issues have rendered the recycling of such waste materials a highly critical subject for protection of natural sources.

Among industrial production, it is remarkable that 150–200 kg steelmaking or high furnace slag are produced per one ton of produced raw steel (Tripathy et al., 2020). Blast furnace slags (BFS) are mainly composed of ceramic based compounds such as SiO_2, Al_2O_3, CaO, MgO and $MgAl_2O_4$ (Gupta et al., 2008; Nath and Kumar, 2013; Chang et al., 2015; Tan et al., 2018). Such oxide contents render blast furnace slags (BFS), which are considered as by-product to replace virgin raw material and to conserve the natural resource that is also beneficial for the circular economy.

One of the most common reutilization of industrial slag is its recycling as a sustainable source in construction (FernandezJimenez and Puertas, 1997; Turner and Collins, 2013) and ceramic industry (Nadirov et al., 2013; Teo et al., 2014; Guo et al., 2016; Abisheva et al., 2017; Potysz et al., 2018). Exploitation of slag has been extended to biomedical applications such as bone replacement, dental and orthopaedic applications (Stamboulis et al., 2005).

The agricultural activity is other of the most significant source of by-product production. Nowadays, rice is cultivated over 100 countries and consumed by more than half of the world's population. In the past 20 years, the output of rice increased by almost 50% (Zou and Yang, 2019; Jittin et al., 2020). The rice husk (RH) accounts the 20–21% of the total seed weight of rice kernel and large quantities of RH are produced as by-

products, i.e. ca. 41.64 million tons of RH are generated in China alone (Zou and Yang, 2019).

Before rice is used in the food industry, the rice husk is first separated from the grain and rice husk ash (RHA) is produced during its combustion. The RHA constitutes an environmental problem due to air and water pollution associated. Its content in SiO_2 varies from 87 to 97%, depending on the burning conditions, the rice variety, the climate and the geographic area (Kordatos et al., 2013). Due to its low cost and high silica content, RHA could be used as an alternative cheap source of silica in the preparation of several products such as i) adsorbent of organic dye and inorganic metals (Feng et al., 2004; Srivastava et al., 2008; Lakshmi et al., 2009), and, ii) starting material for the production of concrete, and silicates (Krishnarao and Godkhindi, 1992; SIE, 1994; Kamath and Proctor, 1998; Kalapathy et al., 2000, 2003; Nehdi et al., 2003; de Sensale, 2006; Ganesan et al., 2008; Chindaprasirt et al., 2009; Salas et al., 2009; Bhagiyalakshmi et al., 2010; Saceda et al., 2011).

Swelling high charged micas, Na-Mica-*n* (*n* is the layer charge and originated by Si^{+4}/Al^{+3} substitutions) have stood out as an attractive adsorbent for its unique combination of high charge and swelling and cation exchange properties (Komarneni et al., 2005; Alba et al., 2006; Choi et al., 2009; Noh et al., 2013; Kim et al., 2014; Naranjo et al., 2015). However, up to now, very pured commercial reagents have been used for their preparation. Thus, feasible and economical scalable synthesis methods are being investigated for the technical applications of those synthetic micas. For example, the parameters (time, temperature and oven) that obtained the most sustainable synthesis, appropriate to large-scale applications have been stablished(Osuna et al., 2018). However, it is still a goal to find more cost-effective aluminosilicate sources for future large-scale applications.

The use of natural clay and/or by-products for the mica synthesis could provide an opportunity to produce an added-value productand to obtain a sustainable, no pollution and zero emissions production. However, despite the high potential of blast furnace slag and/or rice husk ash utilization for the synthesis of these materials, up to our knowledge, no studies have been reported yet. The current study investigates the fabrication of Na-Mica-*n* from FEBEX bentonite, blast furnace slag and rice husk ash as precursors. The synthesis yield, mica types and structural characteristics have been studied thorough X-ray Diffraction and Solid State Nuclear Magnetic Resonance.

2. Experimental

2.1. Starting materials

The starting materials were SiO_2, $Al(OH)_3$, MgF_2, NaCl, a natural clay mineral, FEBEX bentonite, and some industrial wastes such as blast furnace slag (BFS), raw ash rice husk (RHA) and calcined ash rice husk (CRHA) (Table S1).

The commercial reagents were purchased by Sigma-Aldrich (SiO_2 99.8% of purity, CAS n° 112945-52-5; $Al(OH)_3$ 80.5% of purity, CAS n° 21645-51-2; and; MgF_2 56.9% of MgO, CAS n° 7783-40-6)and from Panreac (NaCl 99.5% of purity, CAS n° 131,659).

FEBEX bentonite was extracted from the Cortijo de Archidona deposit (Almería, Spain). The processing at the factory consisted of disaggregation and gently grinding, drying at 60 °C and sieving by 5 mm. The montmorillonite content was 90–92% (Fernandez et al., 2004). Based on chemical analyses, the structural formula or unit-cell formula of the Ca conditioned FEBEX smectite is:

$(Ca_{0.5}Na_{0.08}K_{0.11})(Si_{7.78}Al_{0.22})(Al_{2.78} Fe^{III}_{0.33}Fe^{II}_{0.02}Mg_{0.81})O_{20}(OH)_4$ (Fernandez et al., 2004).

The BFS industrial waste come from Tudela Veguín (Oviedo) blast furnace slag after slow cooling in air and without water with a 36.0% of SiO_2 (Rios et al., 2020).

The raw rice husk ash (RHA), with a 74.1% of SiO_2, comes from the facilities of the rice producer Arroces Herbá settled in Seville, Spain (Cifuentes et al., 2012). The CRHA precursor was prepared by the thermal treatment of RHA at 700 °C, 5°/min, for 2 h to remove organic contains and to increase the SiO_2 contain up to a 94.7% (Roschat et al., 2016).

2.2. Synthesis of Na-Mica-n

For the synthesis of Na-Mica-*n* (*n* = 2 or 4), the NaCl melt method was followed regardless the nature of the precursors (Alba et al., 2006). The general procedure consisted on the use of a (4-*n*)Si: *n*Al: 6 Mg: 2*n*Na powdered mixture. The starting mixtures were grounded in an agate mortar and heated in a Pt crucible at 900 °C, 15 h at 10 °C/min. The heated solids were cooled down to room temperature (RT) and washed with distilled water. The nature of the precursors and the sample nomenclatures were summarized in Table 1.

2.3. Characterization

X-ray diffraction (XRD) patterns were obtained at the X-ray laboratory (CITIUS, University of Seville, Spain) on a Bruker D8 Advance instrument equipped with a Cu K$_\alpha$ radiation source operating at 40 kV and 30 mA. Diffractograms were measured in the range 3–70° 2θ, with step time of 0.1 s and step size of 0.015°.

Single-pulse (SP) MAS NMR experiments were recorded on a Bruker AVANCE WB400 spectrometer equipped with a multinuclear probe. Powdered samples were packed in 3.2 mm zirconia rotors and spun at 10 kHz. ^{29}Si MAS NMR spectra were acquired at a frequency of 79.49 MHz, pulse width of 2.7 μs (π/6) each 3 s. ^{27}Al MAS NMR spectra were recorded at 104.26 MHz with a pulse of 0.38 μs (π/20) and a delay time of 0.5 s. ^{23}Na MAS NMR spectra were recorded at 105.84 MHz with a pulse of 0.75 μs (π/12) and a delay time of 0.1 s. ^{19}F MAS NMR spectra were obtained using typical π/2 pulse of 2.9 μs and a pulse space of 2 s. The chemical shift values were reported in ppm from tetramethylsilane for ^{29}Si, from NaF for ^{19}F and from a 0.1 M $AlCl_3$ and NaCl solution for ^{27}Al and ^{23}Na, respectively. Spectra were simulated using the DMFIT software (Massiot et al., 2002) and Gaussian-Lorenztian ratio, position, linewidth and amplitude were the fitted parameters.

3. Results and discussion

3.1. Use of by-products of different industrial activity

Fig. 1 shows the XRD patterns of the Na-Mica-*n* synthesized from commercial products (Alba et al., 2006) and those synthesized using by-products for replacing part of the commercial precursors.

Na-Mica-*n* synthesized from commercial products showed patterns (Fig. 1a and e) that correspond to swelling high-charged micas (Naranjo et al., 2015) with a unique *001* reflection corresponding to a basal space of 1.21 nm due to hydrated Na^+ in the interlayer spacing of micas (Pavón et al., 2013). The XRD patterns of the samples synthesized from blast furnace slag (Fig. 1b and f) only showed a very small reflection of basal spacing at 0.97 nm due to collapsed 2:1 phyllosilicate (Grim, 1968). The main reflections of these XRD patterns were due to two silicates: i) a nesosilicate, consisting of isolated silicon tetrahedra, forsterite ($Mg_{1.8}Fe_{0.2}SiO_4$, PDF 00-010-0062); and; ii) a sorosilicate, consisting of double tetrahedra with a shared oxygen vertex, cuspidine ($Ca_4Si_2O_7F_{1.5}(OH)_{0.5}$, PDF 01-076-0062). In addition to those silicates, other crystalline impurities such as fluorite (CaF_2, PDF 00-004-0864) and $MgAlO_4$ (PDF 00-010-0062) were observed.

In samples synthesized from raw or calcined rice husk ash, the main crystalline phase of the XRD patterns (Fig. 1c, d, g and h) was a 2:1 phyllosilicate. The main *001* reflection corresponded to a basal spacing of 1.21 nm due to hydrated Na^+ in the interlayer space (Pavón et al., 2013) and it was accompanied by a reflection at ca. 0.97 nm basal spacing due to non-hydrated Na^+ in the interlayer space (Grim, 1968). The non-hydrated/hydrated layers ratio was higher in Mica-2 patterns than in Mica-4 patterns, and in both the dehydration state of the layers

Table 1
Amount of the reagent that participate in the synthesis and sample names.

Sample name	BFS (mg)	RHA (mg)	CRHA (mg)	FEBEX (mg)	SiO$_2$ (mg)	Al(OH)$_3$ (mg)	MgF$_2$ (mg)	NaCl (mg)
Na-M4	–	–	–	–	792.2	1304.9	1369.5	1533.4
M4-BFS-1	1956.4	–	–	–	–	708.8	980.8	1354.1
M4-BFS-2	794.5	–	–	794.5	–	856.2	1132.7	1422.0
M4-RHA	–	1005.1	–	–	–	1241.3	1294.8	1458.7
M4-CRHA	–	–	822.42	–	–	1298.3	1353.5	1525.7
M4-FEBEX[a]	–	–	–	1307.1	–	852.7	1296.1	1544.0
Na-M2	–	–	–	–	597.6	328.1	688.7	385.6
M2-BFS-1	1185.6	–	–	–	70.0	–	428.6	315.8
M2-BFS-2	525.5	–	–	525.5	64.5	–	538.4	346.0
M2-RHA	–	726.9	–	–	–	299.2	622.3	351.6
M2-CRHA	–	–	617.6	–	–	325.0	675.4	381.9
M2-FEBEX[a]	–	–	–	920.8	53.4	–	644.0	381.8

[a] synthesized in a Al$_2$O$_3$ crucible.

increased when calcined rice husk ash was used as starting material. Small reflections of impurities such as forsterite, in Mica-2, and, palygorskite (a fibrous magnesium aluminium phyllosilicate, PDF 00-021-0958), in Mica-4, were observed.

The higher mica yields in the synthesis from rice husk ash (RHA and CRHA) were quite well correlated with the percentage of the mica heteroatoms in the starting materials (ca. 55%*w/w* in BFS vs ca. 75%*w/w* and ca. 95%*w/w* in RHA and CRHA, respectively).

To ensure the efficiency of the Al framework incorporation and the Si-Al tetrahedral distribution, the ^{29}Si MAS NMR spectra were analysed. In Na-Mn samples, the spectra (Fig. 2a, left) consisted in a set of signals on the −70 to −95 ppm region due to Q^3(mAl) ($3 \leq m \leq 0$) mica environments (Alba et al., 2006). The area of each ^{29}Si Q^3(mAl) signals (Table S2 and S3) was the same than previously reported for Na-Mica-n (Alba et al., 2006). The Na-M4 spectrum exhibied two Q^3(3Al) environment which could be due to Lowenstein rule violation (Pavón et al., 2014b) or different octahedral sheet environment (Sanz and Serratosa, 1984). The Na-M2 spectrum showed also other two signals of impurities (Table S2): i) a signal at ca. −85 ppm due to Q^4(4Al) from sodalite (Johnson et al., 2000; Naranjo et al., 2014) that implied the 8.1% of total Si; and ii) a signal at ca. −62 ppm due to Q^0 from forsterite (Kanzaki and Xue, 2016) and that implied the 3.3% of total Si.

The Mn-BFS-1 spectra (Fig. 2b, left) were characterized by a set of signals in the −70 to −95 ppm region, being the main signal at ca. −80 ppm Si Q^3(2Al) environment, (Alba et al., 2006).

These signals can be attributed to Q^3(mAl) ($3 \leq m \leq 0$) environments from two set of 2:1 phyllosilicates with different layer charge, as derived from their chemical shifts and the relative intensity of the signals (Sanz and Serratosa, 1984). In addition to the Q^3(mAl) signals, two other signals due to impurities were observed: i) a signal at ca. −72 ppm due to gehlenite (Florian et al., 2012), accounting the 3.6% and 5.9% of total Si for M2-BFS-1 and M4-BFS-1, repectively; and; ii) a signal at ca. −75 ppm due to cuspidine (Li et al., 2015) and that overlapped with Q^3(3Al) environment. It is also observable a signal at ca. 62 ppm due to forsterite (Kanzaki and Xue, 2016). This last accounted for 13.9% and 35.2% of total Si for M2-BFS-1 and M4-BFS-1, respectively (Table S2 and S3).

The ^{29}Si MAS NMR spectra of M2-RHA and M2-CRHA (Fig. 2c and d, up-left) were quite similar and characterized by the same set of signals than Na-M2 (Fig. 2a, up-right) but with a different relative intensity of the Q^3(mAl) environments (Table S2). These signals resonated almost at the same chemical shift, thus, the change in the relative intensities could not be due to a change in the layer charge but in the distribution of the Si and Al in the tetrahedral sheet (Naranjo et al., 2015). The highest mica yield was for M2-CRHA (82.5% of total Si in comparison with 79.5% and 68.0% for Na-M2 and M2-RHA, respectively, Table S2).

The ^{29}Si MAS NMR spectra of M4-RHA and M4-CRHA (Fig. 2c and d, down-left) were also quite similar to that of Na-M4 (Fig. 2a, down-left). The main signal was a convolution of two set of Q^3(mAl) ($3 \leq m \leq 0$) environments of 2:1 phyllosilicates with different layer charge, Table S3,

as derived from their chemical shifts and the relative intensity of the signals (Sanz and Serratosa, 1984). In addition, other signals due to impurities were also observed: i) four signals at ca. −78 ppm, ca. −82 ppm, ca. −85 ppm and ca. −86 ppm due to pargasite (Welch et al., 1994), being its contribution smaller in M4-RHA than in M4-CRHA; and; ii) a signal at ca. −75 ppm due to cuspidine (Li et al., 2015) which overlapped with Q^3(3Al) environment. Moreover, the Q^0 environment of forsterite, at ca. -62 ppm (Kanzaki and Xue, 2016), was also observed, being its intensity lower in M4-CRHA than in M4-RHA.

Due to the overlap of the different environments in ^{29}Si MAS NMR spectra in Mica-4 samples, the starting material influence could only be analysed in Mica-2. It was observed that the total amount of Si Q^3(mAl) environments (78.2% and 73.2% for RHA and CRHA respectively) and Si/Al of Mica-2 (Si/Al = 2.5 for both) decreased when rice husk ash was used instead of the commercial reagents (88.6% and Si/Al = 2.9).

The ^{27}Al MAS NMR spectra of Na-Mn samples (Fig. 2a, right) showed a main signal at ca. 65 ppm due to the majority of Al in a tetrahedral coordination (Engelhardt and Michel, 1987) and an additional small signal at ca. 0 ppm that was interpreted as aluminium in the octahedral sheet (Naranjo et al., 2014). The spectra of the Mn-BFS-1 (Fig. 2b, right) showed also an additional signal at 0 ppm compatible with MgAlO$_4$ impurity detected by XRD (Blaakmeer et al., 2015), more evident for n = 4 than n = 2. The signal at ca. 65 ppm was not asymmetric as observed for aluminium in Na-Mn and it could be deconvoluted into two signals, the q^3(0Al) signal from mica (Engelhardt and Michel, 1987) and aluminium of gehlenite already observed by ^{29}Si MAS NMR spectroscopy (Florian et al., 2012). The ^{27}Al MAS NMR spectra of Mn-RHA and Mn-CRHA (Fig. 2c and d, right) were similar to that of the original Na-Mn (Fig. 2a).

Although the XRD data of Na-Mn micas (Fig. 1a) was compatible with hydrated interlayer sodium, the difference in the coordination sphere of the interlayer sodium can only be analysed by a ^{23}Na MAS NMR spectroscopy (Fig. 3a, left). The spectrum of Na-M4 (Fig. 3a, down-left) was characterized by a unique symmetrical signal centred at ca. −7.5 ppm compatible with the interlayer sodium in one-layer hydrated state (Naranjo et al., 2014). A similar signal was observed in Na-M2 spectrum (Fig. 3a, up-left), together with a peak at ca. 25 ppm due to non-exchangeable sodium (Zeng et al., 2013).

The spectra of the samples synthesized from BFS (Fig. 2b, left) exhibited a very small signal in the range 0 to −25 ppm due to the low yield of the 2:1 phyllosilicate synthesis, as observed by XRD. This signal was very broad and asymmetric due to the presence of dehydrated sodium (Laperche et al., 1990). A signal at ca. 5 ppm due to sodalite (Johnson et al., 2000) was also observed.

^{23}Na MAS NMR spectra of Mn-RHA and Mn-CRHA (Fig. 2c and d, left) were characterized by two signals in the range 0 to −30 ppm: i) a main signal at ca. −7.5 ppm compatible with one-layer hydrated sodium in the interlayer space (Naranjo et al., 2014); and; ii) a signal at ca. −20 ppm due to dehydrated sodium (Laperche et al., 1990). The ratio
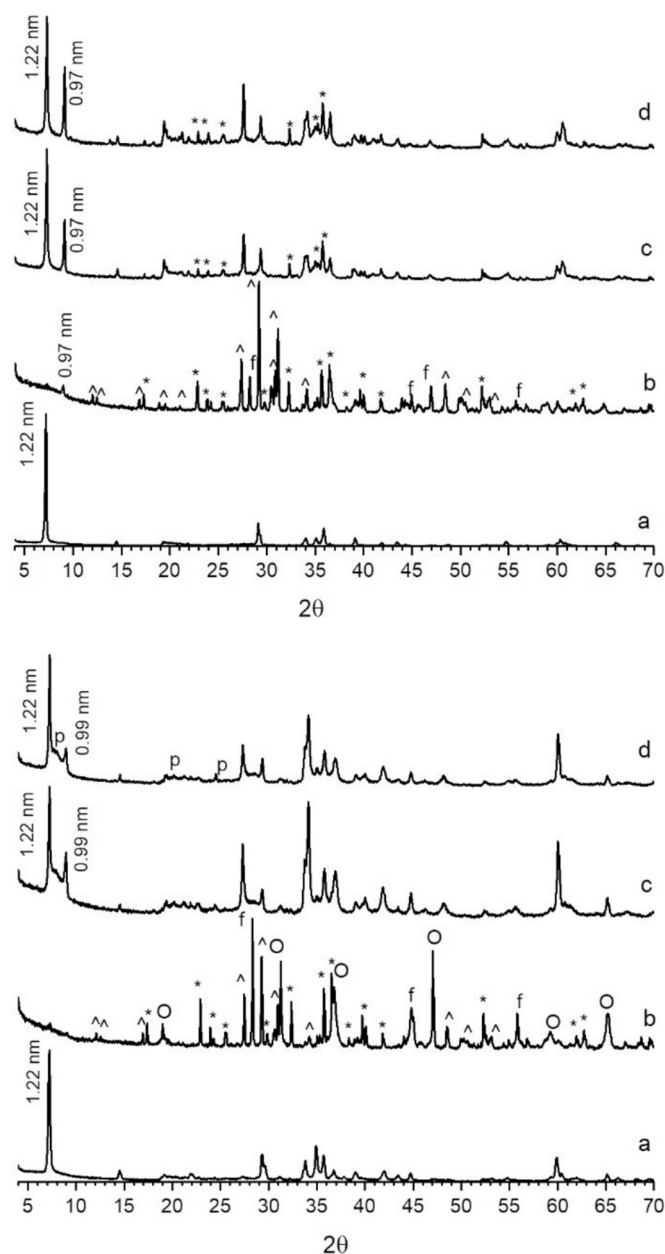
Fig. 1. XRD of a) Na-M2, b) M2-BFS-1, c) M2-RHA, d) M2-CRHA, e) Na-M4, f) M4-BFS-1, g) M4-RHA, and, h) M4-CRHA. * = forsterite, $Mg_{1.8}Fe_{0.2}SiO_4$ (PDF 01-079-2185); O=$MgAlO_4$ (PDF 00-010-0062); f = fluorite, CaF_2 (PDF 00-004-0864); ^=cuspindine, $Ca_4Si_2O_7F_{1.5}$ $(OH)_{0.5}$ (PDF 01-076-0624); and; p = palygorskite, $(Mg,Al)_5(Si,Al)_8O_{20}(OH)_2 \cdot 8H_2O$ (PDF 00-021-0958).

between both signals agreed with the XRD data (Fig. 1c and d). Additionally, the spectra of M2-RHA and M2-CRHA showed the peak at ca. 25 ppm due to non-exchangeable sodium (Zeng et al., 2013) and the spectra of M4-RHA and M4-CRHA showed a narrow peak at ca. 5 ppm due to sodalite (Johnson et al., 2000).

^{19}F MAS NMR spectra of Na-Mn showed two set of signals (Fig. 3a, right), one of higher intensity centered at ca. -177 ppm due to the F-3 Mg environment (Cattaneo et al., 2011) and a second signal centered at -182 ppm that corresponded to the F-2 Mg-1Na environment (Cattaneo et al., 2011). This sodium in the octahedral sheet corresponded to the non-exchangeable sodium detected by ^{23}Na MAS NMR (Fig. 3a, left). The proportion of the F-2 Mg-1Na environment depended on the layer charge (Table S4 and S5), being 7.1% for Na-M2 and 0.3% for Na-M4 in concordance with the high content of non-exchangeable sodium in Na-
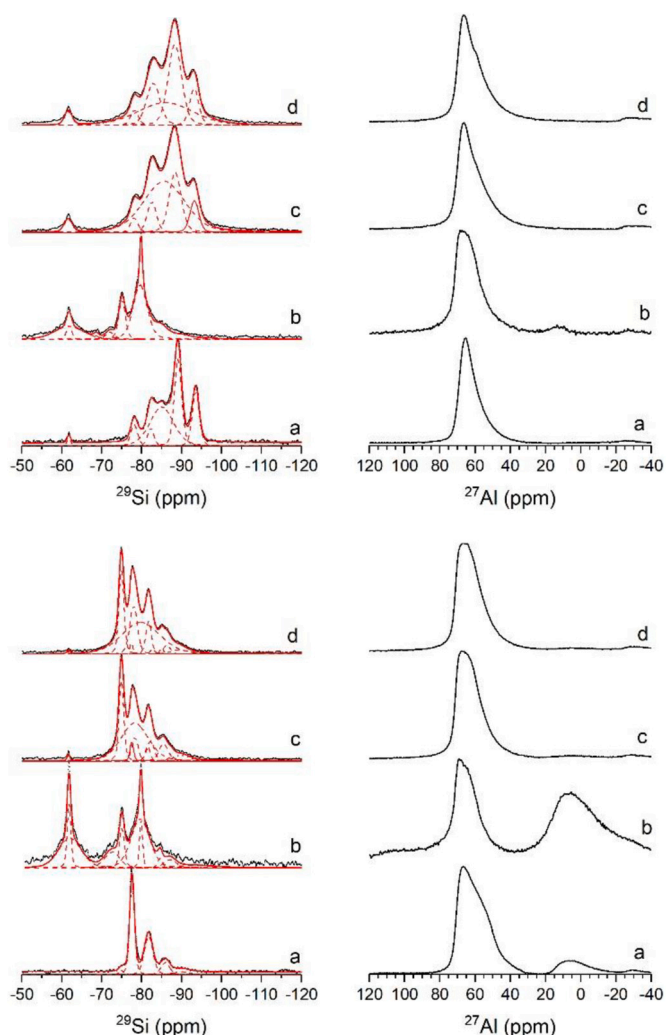

Fig. 2. ^{29}Si (left) and ^{27}Al (right) MAS NMR spectra of Na-Mica-n ($n = 2$, up, and, $n = 4$, down): a) Na-Mn, b) Mn-BFS-1, c) Mn-RHA, and, d) Mn-CRHA.

M2 (Fig. 3a, left). Both signals could be deconvoluted into four resonances, due to the structural arrangement of Mg in the octahedral sheet. Mg cations are located in the center of the octahedral gap and fluorine ions could be placed in cis or trans configuration (Cattaneo et al., 2011). Moreover, mica had hydroxyl groups that could replace F^- in the octahedral sheet. Therefore, there were four possible configurations for each fluorine ion environment: F-Mg-F (cis), F-Mg-F (trans), F-Mg-OH (cis) and F-Mg-OH (trans) and, therefore, each ^{19}F signal was broken down into 4 signals (Cattaneo et al., 2011).

When blast furnace slag was used in the starting synthesis mix, a new set of signals at ca. -105 ppm was observed in the ^{19}F MAS NMR spectra of Mn-BFS-1 (Fig. 3b, right) that can be deconvoluted into two signals at ca. -102 ppm and ca. -107 ppm due to the impurities of cuspidine and CaF_2 (Jain et al., 2010; Tran et al., 2012). It is remarkable the absence of the signal centered at -182 ppm due to F-2 Mg-1Na environment as consequence of the absence of non-exchangeable sodium on those samples (Fig. 3b, left).

^{19}F MAS NMR spectra of M2-RHA and M2-CRHA exhibited three signals (Fig. 3c and d, up-right, Table S4): i) at ca. -171 ppm that could be due to a vacancy ($\square$) produced by the leaching of Mg^{2+}or Na^+ (F-2 Mg-$\square$), ii) at ca. -177 ppm due to F-3 Mg environment and, iii) at ca. -182 ppm due to F-2 Mg-1Na environment (Reinholdt et al., 2005; Cattaneo et al., 2011). The proportion of each fluorine environment was independent of the pre-synthesis treatment of the ash rice husk. On the contrary, ^{19}F MAS NMR spectra of M4-RHA and M4-CRHA exhibited
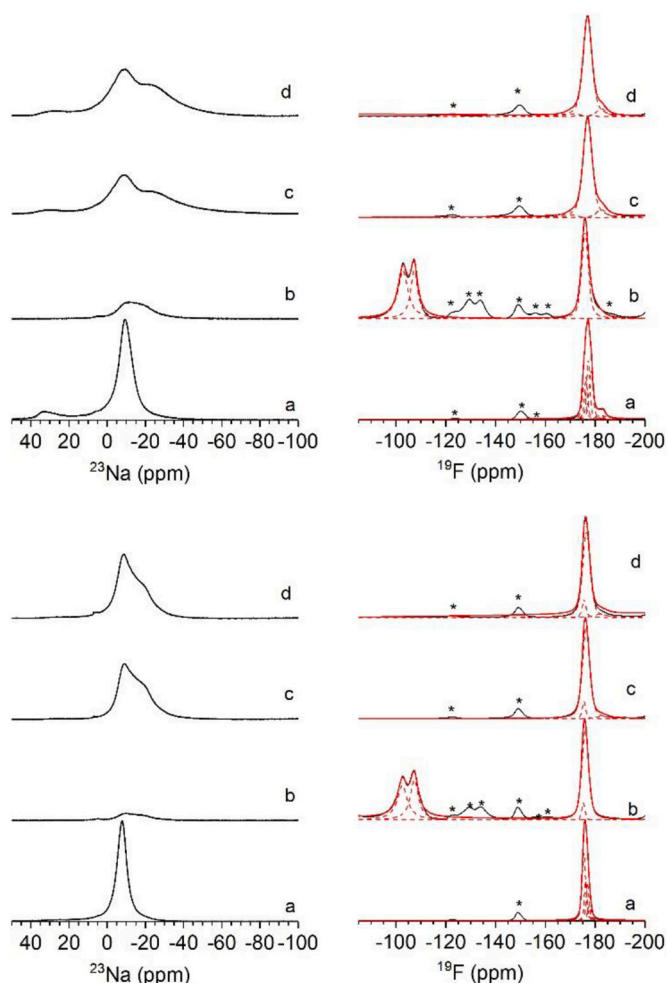
Fig. 3. ^{23}Na (left) and ^{19}F (right) MAS NMR spectra of Na-Mica-*n* (*n* = 2, up, and, *n* = 4, down): a) Na-M*n*, b) M*n*-BFS-1, c) M*n*-RHA, and, d) M*n*-CRHA. * = spinning side bands.

only the two signals (Fig. 3c and d, down-right, Table S5) of F-3 Mg and F-2 Mg-1Na environment.

These results demonstrated that by-products can be good starting materials for the mica synthesis. In fact, the use of those by-products with high SiO$_2$ content (M*n*-CRHA) have favored the reaction yield. Moreover, these micas (M*n*-CRHA) have exhibited structural characteristics and cation framework distribution similar to those synthesized with commercial products (Na-M*n*).

3.2. Use of bentonite in blast furnace slag synthesis formulae of mica

As shown in the previous section, only a minor amount of crystalline non-swelling mica was formed when blast furnace slag, BFS, was used as a precursor (Fig. 2a, Fig. 4a). To improve this result, BFS amount in the synthesis was partially substituted by a bentonite (FEBEX, swelling low-charged phyllosilicate). The XRD diagrams of both M*n*-BFS-2 samples (Fig. 4b) showed patterns similar to Na-M*n* (Fig. 1a and e).

In the XRD patterns, reflections of other silicates such as forsterite (nesosilicate Mg$_{1.8}$Fe$_{0.2}$SiO$_4$, PDF 00-010-0062) and cuspidine (sorosilicate Ca$_4$Si$_2$O$_7$F$_{1.5}$(OH)$_{0.5}$, PDF 01-076-0062) for both M*n*-BFS-2 samples, and, pargasite (inosilicate NaCa$_2$(Mg$_4$Al)Si$_6$Al$_2$(OH)$_2$, PDF 01-087-0607) for M2-BFS-2 (Fig. 2b, up) were also observed. In addition to these silicates, other crystalline impurities such as fluorite (CaF$_2$, PDF 00-004-0864) and halite (K$_{0.2}$Na$_{0.8}$Cl, PDF 00-026-0918) were also detected.

^{29}Si MAS NMR spectra of the M*n*-BFS-2 (Fig. 5b, left) showed a set of

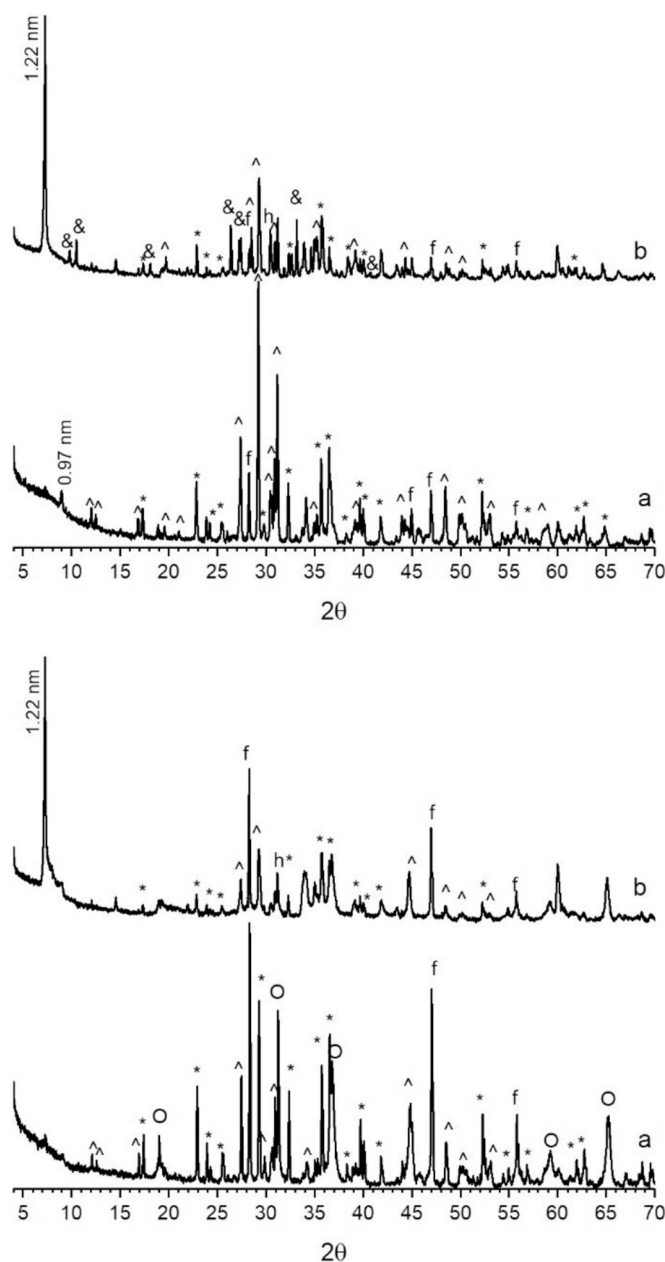**Fig. 4.** XRD of M*n*-BFS (*n* = 2, up, and, *n* = 4, down): a) M*n*-BFS-1, and, b) M*n*-BFS-2. * = forsterite, Mg$_{1.8}$Fe$_{0.2}$SiO$_4$ (PDF 01-079-2185); O═MgAlO$_4$ (PDF 00-010-0062); f = fluorite, CaF$_2$ (PDF 00-004-0864); ^=cuspidine, Ca$_4$Si$_2$O$_7$F$_{1.5}$(OH)$_{0.5}$ (PDF 01-076-0624); & = pargasite, NaCa$_2$(Mg$_4$Al)Si$_6$Al$_2$(OH)$_2$ (PDF 01-087-0607); and, h = halite, K$_{0.2}$Na$_{0.8}$Cl (PDF 00-026-0918).

signals centred in the same range than those of M*n*-BFS-1 (Fig. 5a, left). The gravity centre of the spectra shifted to higher frequency indicating an enrichment in the Q^3(mAl) environments with higher *m* value (Alba et al., 2006). Moreover, due to the contribution of additional signals of pargasite, the spectra were broader than Mn-BFS-1 (Welch et al., 1994). The Q^3(0Al) and Q^3(1Al) signals of M*n*-BFS-2 resonated at higher frequency than those of bentonite FEBEX; moreover, the spectra also exhibited also resonances of Q^3(2Al) and Q^3(3Al), absent in the ^{29}Si MAS NMR spectrum of pristine bentonite (Osuna et al., 2015). Thus, the structural short-range arrangement of Si pointed out the transformation of FEBEX (a low charged 2:1 phyllosilicate) to a high charged mica. Finally, the intensity of Q^0 signals of forsterite remained almost constant in M2-BFS but decreased in M4-BFS-2 respect to M4-BFS-1 (Table S2 and S3).
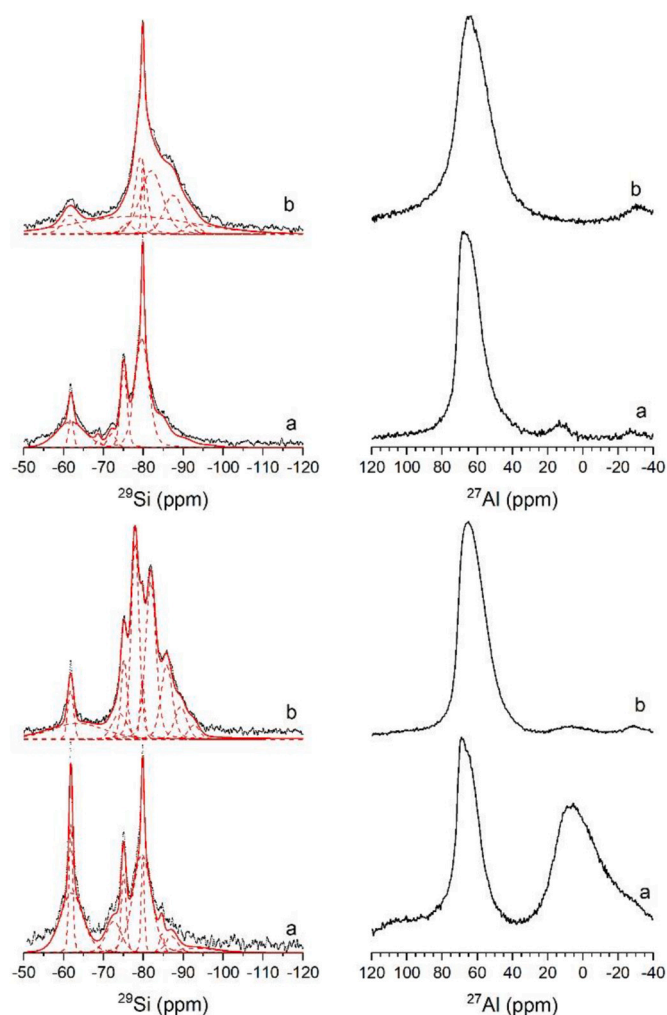
Fig. 5. ^{29}Si (left) and ^{27}Al (right) MAS NMR spectra of Mn-BFS ($n = 2$, up, and, $n = 4$, down): a) Mn-BFS-1, and, b) Mn-BFS-2.

Fig. 6. ^{23}Na (left) and ^{19}F (right) MAS NMR spectra of Mn-BFS ($n = 2$, up, and, $n = 4$, down): a) Mn-BFS-1, and, b) Mn-BFS-2. * = spinning side bands.

^{27}Al MAS NMR spectra of the Mn-BFS-2 (Fig. 5b, right) showed a line shape completely different to those of Mn-BFS-1 (Fig. 5a, right). In them, only a broad symmetric signal at ca. 65 ppm due to q^3(0Al) of phyllo-silicate 2:1 is observable together with the peak attributable to the impurity of pargasite (Welch et al., 1994). This indicated the migration of the octahedral aluminium typical of bentonite FEBEX (Osuna et al., 2015) to tetrahedral positions in the mica structure.

^{23}Na MAS NMR spectra of the samples synthesized from BFS and bentonite (Fig. 6b, left) were very similar to those of the samples synthesized without bentonite (Fig. 6a, left). The signal in the range between 0 to −25 ppm, due to interlayer sodium at different hydration state, (Laperche et al., 1990) increased in M4-BFS-2 and decreased in M2-BFS-2. In both Mn-BFS-2 the signal at ca. 5 ppm due to sodalite was absent.

^{19}F MAS NMR spectra of the micas synthesized with bentonite and blast furnace slag, Mn-BFS-2 (Fig. 6b, right) exhibited the same signals than the Mn-BFS-1 spectra (Fig. 6a, right) but with different relative intensities (Table S4 and S5). The substitution of BFS by bentonite increased, the intensity of the ^{19}F signals from impurities for M2-BFS-2 (Table S4) while those signals decreased for M4-BFS-2 (Table S5).

All these results indicated that the partial substitution of BFS by bentonite FEBEX not only significantly increased the reaction yields but also the efficiency in the aluminium incorporation into the tetrahedral sheet and the layer hydration. Two different factors can be identified as
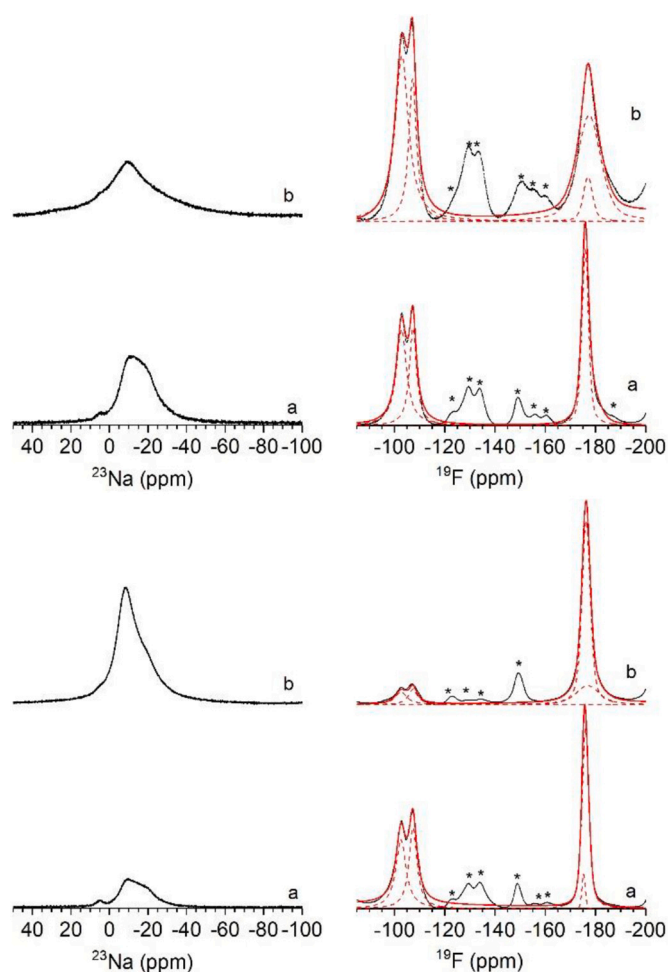
responsible of this fact: i) an increase in SiO$_2$ content and, ii) as shown by MAS-NMR, Si environment in bentonite is similar to Q^3 environment in mica; by contrast, BFS exhibits Q^4 environments.

3.3. Use of bentonite for mica synthesis

Last, FEBEX bentonite was used as the only source of Si and Al to produce high charged mica. XRD patterns of M2-FEBEX and M4-FEBEX (Fig. 7) were quite different than that of the pristine bentonite (Osuna et al., 2015). They corresponded to sodium mica, with a main reflection of *001* at 1.21 nm compatible with the presence of hydrated sodium in the interlayer space (Pavón et al., 2014a). In the case of M2-FEBEX, a reflection at higher 2Θ values also emerged due to dehydrated mica (Pavón et al., 2014a). In both micas, reflections corresponding to so-dalite and forsterite were also observed.

To check the hydration of the sodium cations in the interlayer space, the samples were analysed by ^{23}Na MAS NMR (Fig. 8). ^{23}Na MAS NMR spectra were characterized by a signal centred at −10 ppm due to hydrated sodium with a shoulder at lower frequency due to a lower hydration state of the mica (Naranjo et al., 2014). The hydrated sodium signal was broader than that of the Na-Mn, indicating the presence of different hydration states of interlayer sodium. A signal was also observed at ca. 5 ppm corresponding to the sodalite (Naranjo et al., 2014), already observed in the XRD diagrams.

To study the short-range structural order, the samples were also analysed by ^{19}F, ^{27}Al and ^{29}Si MAS NMR spectroscopy.
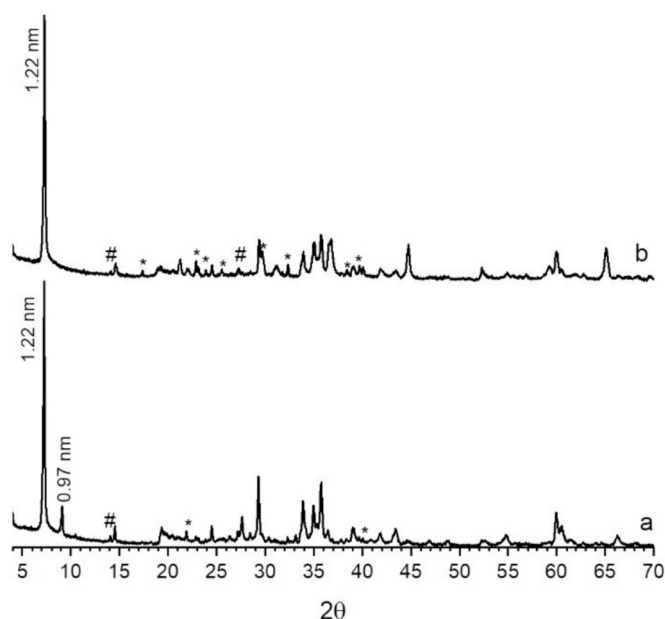
Fig. 7. XRD of a) M2-FEBEX and b) M4-FEBEX. * = forsterite, $Mg_{1.8}Fe_{0.2}SiO_4$ (PDF 01-079-2185) and # = sodalite (PDF 04-008-2098).
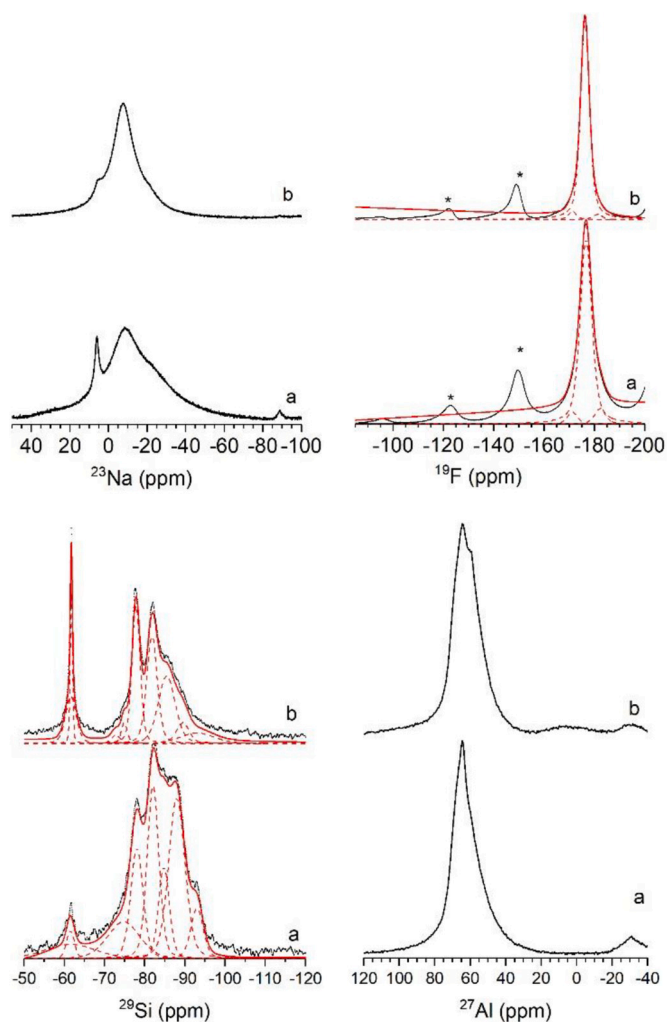
^{19}F MAS NMR spectra (Fig. 8) of Mn-FEBEX showed a main peak at ca. −176 ppm due to F-3 Mg environment, and two small peaks at ca. −182 ppm and ca. −171 ppm due to F-2 Mg-1Na and F-2 Mg-□ environments, respectively (Reinholdt et al., 2005; Cattaneo et al., 2011).

^{29}Si MAS NMR spectrum of M4-FEBEX (Fig. 8b) showed Q^3(mAl) environments distribution slightly different to that of Na-M4 (Fig. 2a, down-left), indicating that the mica had a different tetrahedral framework cations distribution. However, it did not imply a different layer charge since no changes were observed in the chemical shift of the signals (Table S3). On the contrary, the M2-FEBEX spectrum (Fig. 8) presented an enrichment in environments with m ≥ 2 (Table S2). In both micas, the presence of forsterite was also observed, being its contribution much higher in the case of M4-FEBEX.

^{27}Al MAS NMR spectrum of M4-FEBEX (Fig. 8) showed a main signal at ca. 65 ppm due to aluminium with tetrahedral coordination (Engelhardt and Michel, 1987). A superimposed narrow signal corresponding to sodalite was also observed (Naranjo et al., 2014). The signal from octahedral coordinated aluminium (ca. 0 ppm) was less intense than in the Na-M4 spectrum (Fig. 2a, down-right). In the case of M2-FEBEX, the ^{27}Al MAS NMR spectrum was similar to that of mica synthesized by the original method, Na-M2 (Fig. 2a, up-right).

The use of FEBEX bentonite as the only source of Si and Al produced high charged mica. However, cation framework distribution was different from Na-Mn and the layers were not completely hydrated.

4. Conclusions

The synthesis of Na-Mn micas has been achieved using a variety of natural clays and/or by-products as precursors, but the synthesis yields and degree of purity of the mica depends on the nature of those precursors.

The purity of the reagents are crucial for the reaction yields and the formation of mica was favored by the use of rice husk ash instead of blast furnace slag. The partial or total incorporation in the synthesis mix of a low charge 2:1 phyllosilicate favors the yields of mica synthesis, the swelling of the layers and the effectiveness of aluminium incorporation in the tetrahedral sheet.

Therefore, these results open the way for the possible industrialization of design adsorbents using a sustainable synthesis method.

Declaration of Competing Interest

The authors declare that they have no known competing financial interests or personal relationships that could have appeared to influence the work reported in this paper.

Appendix A. Supplementary data

Supplementary data to this article can be found online at https://doi.org/10.1016/j.clay.2021.106292.

References

Abisheva, Z.S., Karshigina, Z.B., Bochevskaya, Y.G., Akcil, A., Sargelova, E.A., Kvyatkovskaya, M.N., Silachyov, I.Y., 2017. Recovery of rare earth metals as critical raw materials from phosphorus slag of long-term storage. Hydrometalurgy 173, 271–282.

Alba, M.D., Castro, M.A., Naranjo, M., Pavón, E., 2006. Hydrothermal reactivity of Na-n-micas (n = 2, 3, 4). Chem. Mater. 18, 2867–2872.

Fig. 8. ^{23}Na, ^{19}F ^{29}Si and ^{27}Al MAS NMR spectra of a) M2-FEBEX and b) M4-FEBEX. * = spinning side bands.

Bhagiyalakshmi, M., Yun, L.J., Anuradha, R., Jang, H.T., 2010. Utilization of rice husk ash as silica source for the synthesis of mesoporous silicas and their application to CO2 adsorption through TREN/TEPA grafting. J. Hazard. Mater. 175, 928–938.

Blaakmeer, E.S. (Merijn), Rosciano, F., van Eck, E.R.H., 2015. Lithium doping of MgAl2O4 and ZnAl2O4 investigated by high-resolution solid state NMR. J. Phys. Chem. C 119, 7565–7577.

Cattaneo, A.S., Bracco, S., Comotti, A., Galimberti, M., Sozzani, P., Eckert, H., 2011. Structural characterization of pristine and modified fluoromica using multinuclear solid-state NMR. J. Phys. Chem. C 115, 12517–12529.

Chang, Q., Li, X., Ni, H., Zhu, W., Pan, C., Hu, S., 2015. Modeling on dry centrifugal granulation process of molten blast furnace slag. ISIJ Int. 55, 1361–1366.

Chen, T.-L., Kim, H., Pan, S.-Y., Tseng, P.-C., Lin, Y.-P., Chiang, P.-C., 2020. Implementation of green chemistry principles in circular economy system towards sustainable development goals: challenges and perspectives. Sci. Total Environ. 716 https://doi.org/10.1016/j.scitotenv.2020.136998.

Chindaprasirt, P., Jaturapitakkul, C., Rattanasak, U., 2009. Influence of fineness of rice husk ash and additives on the properties of lightweight aggregate. Fuel 88, 158–162.

Choi, J., Komarneni, S., Grover, K., Katsuki, H., Park, M., 2009. Hydrothermal synthesis of Mn-mica. Appl. Clay Sci. 46, 69–72.

Cifuentes, H., Leiva, C., Medina, F., Fernandez-Pereira, C., 2012. Effects of fibres and rice husk ash on properties of heated HSC. Mag. Concr. Res. 64, 457–470.

de Sensale, G.R., 2006. Strength development of concrete with rice-husk ash. Cem. Concr. Compos. 28, 158–160.

Elkington, J., 1999. Cannibals with forks: the triple bottom line of twenty-first century business. Capstone. Choice Rev. Online 36, 3997.

Engelhardt, G., Michel, D., 1987. High Resolution Solid State NMR of Silicates and Zeolites. John Wiley and Sons, New York.

Feng, Q., Lin, Q., Gong, F., Sugita, S., Shoya, M., 2004. Adsorption of lead and mercury by rice husk ash. J. Colloid Interface Sci. 278, 1–8.

Fernandez, A.M., Baeyens, B., Bradbury, M., Rivas, P., 2004. Analysis of the porewater chemical composition of a Spanish compacted bentonite used in an engineered barrier. Phys. Chem. Earth 29, 105–118.

FernandezJimenez, A., Puertas, F., 1997. Influence of the activator concentration on the kinetics of the alkaline activation process of a blastfurnace slag. Mater. Constr. 47, 31–42.

Florian, P., Veron, E., Green, T., Yates, J., Massiot, D., 2012. Elucidation of the Al/Si ordering in gehlenite Ca2Al2SiO7 by combined Si-29 and Al-27 NMR spectroscopy/quantum chemical calculations. Chem. Mater. 24, 4068–4079.

Ganesan, K., Rajagopal, K., Thangavel, K., 2008. Rice husk ash blended cement: assessment of optimal level of replacement for strength and permeability properties of concrete. Constr. Build. Mater. 22, 1675–1683.

Grim, R.E., 1968. Clay Mineralogy. New York.

Guo, Z., Zhu, D., Pan, J., Wu, T., Zhang, F., 2016. Improving beneficiation of copper and iron from copper slag by modifying the molten copper slag. Metals (Basel). 6, 1–17.

Gupta, S., French, D., Sakurovs, R., Grigore, M., Sun, H., Cham, T., Hilding, T., Hallin, M., Lindblom, B., Sahajwalla, V., 2008. Minerals and iron-making reactions in blast furnaces. Prog. Energy Combust. Sci. 34, 155–197.

Jain, P., Kim, S., Youngman, R.E., Sen, S., 2010. Direct observation of defect dynamics in nanocrystalline CaF2: results from F-19 MAS NMR spectroscopy. J. Phys. Chem. Lett. 1, 1126–1129.

Jittin, V., Bahurudeen, A., Ajinkya, S.D., 2020. Utilisation of rice husk ash for cleaner production of different construction products. J. Clean. Prod. 263.

Johnson, G.M., Mead, P.J., Dann, S.E., Weller, M.T., 2000. Multinuclear MAS NMR studies of sodalitic framework materials. J. Phys. Chem. B 104, 1454–1463.

Kalapathy, U., Proctor, A., Shultz, J., 2000. Silica xerogels from rice hull ash: structure, density and mechanical strength as affected by gelation pH and silica concentration. J. Chem. Technol. Biotechnol. 75, 464–468.

Kalapathy, U., Proctor, A., Shultz, J., 2003. Silicate thermal insulation material from rice hull ash. Ind. Eng. Chem. Res. 42, 46–49.

Kamath, S.R., Proctor, A., 1998. Silica gel from rice hull ash: preparation and characterization. Cereal Chem. 75, 484–487.

Kanzaki, M., Xue, X., 2016. Cation distribution in Mg-Zn olivine solid solution: a Si-29 MAS NMR and first-principles calculation study. J. Mineral. Petrol. Sci. 111, 292–296.

Kim, J.H., Kim, H.J., Park, M., 2014. Stabilization of alkali earth metal cations in Na-4-mica. Appl. Clay Sci. 101, 272–276.

Komarneni, S., Ravella, R., Park, M., 2005. Swelling mica-type clays: Synthesis by NaCl melt method, NMR characterization and cation exchange selectivity. J. Mater. Chem. 15, 4241–4245.

Kordatos, K., Ntziouni, A., Iliadis, L., Kasselouri-Rigopoulou, V., 2013. Utilization of amorphous rice husk ash for the synthesis of ZSM-5 zeolite under low temperature. J. Mater. Cycles Waste Manag. 15, 571–580.

Krishnarao, R.V., Godkhindi, M.M., 1992. Distribution of silica in rice husks and its effect on the formation of silicon carbide. Ceram. Int. 18, 243–249.

Lakshmi, U.R., Srivastava, V.C., Mall, I.D., Lataye, D.H., 2009. Rice husk ash as an effective adsorbent: evaluation of adsorptive characteristics for Indigo Carmine dye. J. Environ. Manag. 90, 710–720.

Laperche, V., Lambert, J.F., Prost, R., Fripiat, J.J., 1990. High-resolution solid-state NMR of exchangeable cations in the interlayer surface of a swelling mica - NA-23, CD-111, and CS-133 vermiculites. J. Phys. Chem. 94, 8821–8831.

Li, J., Yan, B., Shu, Q., Chou, K., 2015. Structure and crystallization kinetics of glassy CaO-Al2O3-SiO2-CaF2-Na2O mold fluxes with varying basicity. Metall. Mater. Trans. B-Process Metall. Mater. Process. Sci. 46, 2458–2469.

Massiot, D., Fayon, F., Lapron, M., King, I., Le Calve, S., Alonso, B., Durand, J.O., Bujoli, B., Gan, Z.H., Hoatson, G., 2002. Modelling one- and two-dimensional solid-state NMR spectra. Magn. Reson. Chem. 40, 70–76.

Nadirov, R.K., Syzdykova, L.I., Zhussupova, A.K., Usserbaev, M.T., 2013. Recovery of value metals from copper smelter slag by ammonium chloride treatment. Int. J. Miner. Process. 124, 145–149.

Naranjo, M., Castro, M.A., Cota, A., Pavón, E., Pazos, M.C., Alba, M.D., 2014. A new route of synthesis of Na-Mica-4 from sodalite. Microporous Mesoporous Mater. 186, 176–180.

Naranjo, M., Castro, M.A.M.A., Cota, A., Osuna, F.J.F.J., Pavón, E., Alba, M.D.M.D., 2015. Synthesis temperature effect on Na-Mica-4 crystallinity and heteroatom distribution. Microporous Mesoporous Mater. 204, 282–288. https://doi.org/10.1016/j.micromeso.2014.11.026.

Nath, S.K., Kumar, S., 2013. Influence of iron making slags on strength and microstructure of fly ash geopolymer. Constr. Build. Mater. 38, 924–930.

Nehdi, M., Duquette, J., El Damatty, A., 2003. Performance of rice husk ash produced using a new technology as a mineral admixture in concrete. Cem. Concr. Res. 33, 1203–1210.

Noh, Y.D., Komarneni, S., MacKenzie, K.J.D., Ro, H.M., Park, M., 2013. Highly charged swelling micas of different charge densities: synthesis, characterization, and selectivity for Sr and Ba. Sep. Purif. Technol. 104, 238–245.

Osuna, F.J., Chain, P., Cota, A., Pavón, E., Alba, M.D., 2015. Impact of hydrothermal treatment of FEBEX and MX80 bentonites in water, HNO3 and Lu(NO3) media: Implications for radioactive waste control. Appl. Clay Sci. 118.

Osuna, F.J., Cota, A., Pavon, E., Alba, M.D., 2018. A comprehensive and in-depth analysis of the synthesis of advanced adsorbent materials. J. Clean. Prod. 194, 665–672.

Pavón, E., Castro, M.A., Naranjo, M., Orta, M.M., Pazos, M.C., Alba, M.D., 2013. Hydration properties of synthetic high-charge micas saturated with different cations: an experimental approach. Am. Mineral. 98, 394–400.

Pavón, E., Castro, M.A., Cota, A., Osuna, F.J., Pazos, M.C., Alba, M.D., 2014a. Interaction of hydrated cations with mica-n (n = 2, 3 and 4) surface. J. Phys. Chem. C 118, 2115–2123.

Pavón, E., Osuna, F.J., Alba, M.D., Delevoye, L., 2014b. Direct evidence of Lowenstein's rule violation in swelling high-charge micas. Chem. Commun. 50.

Potysz, A., van Hullebusch, E.D., Kierczak, J., 2018. Perspectives regarding the use of metallurgical slags as secondary metal resources - a review of bioleaching approaches. J. Environ. Manag. 219, 138–152.

Reinholdt, M., Miehé-Brendlé, J., Delmotte, L., Le Dred, R., Tuilier, M.-H., 2005. Synthesis and characterization of montmorillonite-type phyllosilicates in a fluoride medium. Clay Miner. 40, 177–190.

Rios, J.D., Arenas, C., Cifuentes, H., Vilches, L.F., Leiva, C., 2020. Development of a paste for passive fire protection mainly composed of granulated blast furnace slag. Environ. Prog. Sustain. Energy 39.

Roschat, W., Siritanon, T., Yoosuk, B., Promarak, V., 2016. Rice husk-derived sodium silicate as a highly efficient and low-cost basic heterogeneous catalyst for biodiesel production. Energy Convers. Manag. 119, 453–462.

Saceda, J.-J.F., de Leon, R.L., Rintramee, K., Prayoonpokarach, S., Wittayakun, J., 2011. Properties of silica from rice husk and rice Husk Ash and their utilization for Zeolite Y synthesis. Quim Nova 34, 1394–U289.

Salas, A., Delvasto, S., de Gutierrez, R., Lange, D., 2009. Comparison of two processes for treating rice husk ash for use in high performance concrete. Cem. Concr. Res. 39, 773–778.

Sanz, J., Serratosa, J.M., 1984. Si-29 and Al-27 high-resolution MAS-NMR spectra of phyllosilicates. J. Am. Chem. Soc. 106, 4790–4793.

SIE, S.T., 1994. Past, present and future-role of microporous catalysts in the petroleum-industry. In: Jansen, J.C., Stocker, M., Karge, H.G., Weitkamp, J. (Eds.), Advanced Zeolite Science and Applications, Studies in Surface Science and Catalysis. Elsevier Science BV, Sara Burgerhartstraat 25, PO BOX 211, 1000 Ae Amsterdam, Netherlands, pp. 587–631.

Srivastava, V.C., Mall, I.D., Mishra, I.M., 2008. Removal of cadmium(II) and zinc(II) metal ions from binary aqueous solution by rice husk ash. Colloids Surf. A Physicochem. Eng. Asp. 312, 172–184.

Stamboulis, A., Hill, R.G., Law, R.V., 2005. Crystallisation of apatite stoichiometric ionomer glasses for medical applications and optoelectronics. In: Vaseashta, A., DimovaMalinovska, D., Marshall, J. (Eds.), Nanostructured and Advanced Materials for Applications in Sensor, Optoelectronic and Photovoltaic Technology. NATO Science Series II-Mathematics Physics and Chemistry. Springer, Dordrecht, Netherlands, pp. 395–398.

Tan, Y., Zhu, X., He, X.-Y., Ding, B., Wang, H., Liao, Q., Li, H., 2018. Granulation characteristics of molten blast furnace slag by hybrid centrifugal-air blast technique. Powder Technol. 323, 176–185.

Teo, P.-T., Abu Seman, A., Basu, P., Sharif, N.M., 2014. Recycling of Malaysia's electric arc furnace (EAF) slag waste into heavy-duty green ceramic tile. Waste Manag. 34, 2697–2708.

Tran, T.T., Bildsoe, H., Jakobsen, H.J., Skibsted, J., 2012. Double cross-polarization MAS NMR in the assignment of abundant-spin resonances: F-19-{Si-29}-F-19 FBCP/MAS NMR of fluoride ions incorporated in calcium silicate hydrate (C-S-H) phases. J. Magn. Reson. 221, 19–23.

Tripathy, S.K., Dasu, J., Murthy, Y.R., Kapure, G., Pal, A.R., Filippov, L.O., 2020. Utilisation perspective on water quenched and air-cooled blast furnace slags. J. Clean. Prod. 262.

Turner, L.K., Collins, F.G., 2013. Carbon dioxide equivalent (CO2-e) emissions: a comparison between geopolymer and OPC cement concrete. Constr. Build. Mater. 43, 125–130.

Welch, M., Koloidziejski, W., Klinowski, J., 1994. A multinuclear NMR-study of synthetic pargasite. Am. Mineral. 79, 261–268.

Xie, J., Wu, S., Zhang, L., Xiao, Y., Ding, W., 2016. Evaluation the deleterious potential and heating characteristics of basic oxygen furnace slag based on laboratory and in-place investigation during large-scale reutilization. J. Clean. Prod. 133, 78–87.

Zeng, Z., Matuschek, D., Studer, A., Schwickert, C., Pöttgen, R., Eckert, H., 2013. Synthesis and characterization of inorganic-organic hybrid materials based on the intercalation of stable organic radicals into a fluoromica clay. Dalton Trans. 42, 8585–8596.

Zhang, Y., Liu, J., Su, Z., Liu, B., Lu, M., Li, G., Anderson, C., Jiang, T., 2018. Utilizing blast furnace slags (BFS) to prepare high-temperature composite phase change materials (C-PCMs). Constr. Build. Mater. 177, 184–191.

Zou, Y., Yang, T., 2019. In: Cheong, L.-Z., Xu, X. (Eds.), Chapter 9 - Rice Husk, Rice Husk Ash and their applications. AOCS Press, Rice Bran and Rice Bran Oil, pp. 207–246.